Shape Sensing for Wings with Spars and Ribs using Simulated Strain

Chan-gi Pak[1]
NASA Armstrong Flight Research Center, Edwards, California, 93523-0273, USA

Active trim shape control can be used to minimize error between target and actual aircraft trim shape during flight. Trim shape sensing for aircraft during flight is not only important for highly flexible aircraft, such as the National Aeronautics and Space Administration (NASA) Helios Prototype remotely piloted flying wing aircraft, but also for a delta-wing type aircraft, such as a supersonic commercial transport aircraft. A two-step theory utilizing distributed strain for a real-time shape sensing of a full three-dimensional structure has been introduced previously. This study focuses on the application of the two-step theory to finite element models of a wing with spars and ribs such as the X-59 QueSST aircraft (Lockheed Martin Corporation, Bethesda, Maryland), a tapered wing, a dihedral/anhedral wing, and a stiffened dihedral/anhedral wing. A finely meshed finite element structural model is desired to capture accurate curvature distributions along the neutral axes of the wing cross sections during pre-test analysis for shape sensing of a wing with ribs and spars. The two-step theory used in this study gives excellent deformation correlation with the MSC/NASTRAN (MSC Software, Newport Beach, California) results along the neutral axis for all test cases used in this study except the X-59 QueSST aircraft.

I. Nomenclature

Acronyms

CG	=	center of gravity
DOF	=	degrees of freedom
FE	=	finite element
QueSST	=	Quiet SuperSonic Technology

Symbols

$\{\tilde{\boldsymbol{q}}_{\boldsymbol{M}}(\boldsymbol{t})\}$	=	measured master degrees of freedom at time (t)
$\{\boldsymbol{q}(\boldsymbol{t})\}$	=	generalized displacement vector at time (t)
$\{\boldsymbol{q}_{\boldsymbol{M}}(\boldsymbol{t})\}$	=	master degrees of freedom at time (t)
$\{\boldsymbol{q}_{\boldsymbol{S}}(\boldsymbol{t})\}$	=	slave degrees of freedom at time (t)
α	=	local angle due to wing taper or dihedral/anhedral effects
β	=	local sweep angle due to curvilinear sensor line effects
$\tilde{s}$	=	distance along the neutral axis direction, inch
h($\tilde{s}$)	=	wing thickness at $\tilde{s}$, inch
$[\boldsymbol{T}]$	=	transformation matrix
$w(\tilde{s})$	=	deflection at $\tilde{s}$, inch
$\theta(\tilde{s})$	=	slope at $\tilde{s}$, radian
$\epsilon_l(\tilde{s})$	=	axial strain at $\tilde{s}$ on the lower skin
$\epsilon_u(\tilde{s})$	=	axial strain at $\tilde{s}$ on the upper skin
$\kappa(\tilde{s})$	=	curvature at $\tilde{s}$, in-1 ($\equiv -(\epsilon_u - \epsilon_l)/h$)
$\boldsymbol{\Phi}_{\boldsymbol{M}}$	=	eigen-matrix corresponds to master degrees of freedom
$\boldsymbol{\Phi}_{\boldsymbol{S}}$	=	eigen-matrix corresponds to slave degrees of freedom
$(*)^T$	=	transpose of a matrix
$(*)^{-1}$	=	inverse of a matrix

[1]Senior Aerospace Engineer, Aerostructures Branch, Senior Member AIAA.

II. Introduction

The NASA Helios Prototype remotely piloted flying wing aircraft experienced a total structural failure 30 minutes after takeoff at the island of Kauai, Hawaii, on June 26, 2003. Before the mishap, the aircraft faced turbulence and started a divergent pendulum motion in the pitch direction caused by a high center of gravity (CG) location and the "persistent" high dihedral configuration [1]. Aeroelastic stability analysis of the aircraft was performed during the mishap investigation. This analysis showed that one of flexible modes of the aircraft became highly damped at zero frequency, i.e., an over-damped response to external loads, before the mishap; see page 41 of Ref. [1]. Based on this over-damped structural behavior, the following two recommendations were prepared:

1) Develop a method to measure wing dihedral in real-time with a visual display available to the test crew. (Recommendation R.11, page 93 of Ref. [1].)
2) Develop manual and/or automatic techniques to control wing dihedral in flight. (Recommendation R.12, page 93 of Ref. [1].)

Trim shape sensing for an aircraft during flight is not only important for highly flexible aircraft such as the NASA Helios, but also for stiff delta wing configurations, such as a supersonic commercial transport aircraft [2]. The outer-mold-line configuration of a supersonic commercial transport aircraft is designed for a desired aerodynamic performance, such as low-boom, using a rigid structural assumption. Actual in-flight trim shape, however, differs from the target trim shape (an outer-mold-line shape plus trim variable effects) due to the flexibility of the structure of an aircraft. A jig shape optimization technique was proposed to minimize errors between the target trim shape and the actual trim shape [3]. The updated jig shape, however, is optimum only at the design flight condition; to overcome this limitation, an active trim shape control technique can be used to minimize the error between the target and the actual trim shapes during flight.

The trim shape of an aircraft must be measured during flight in order to implement active trim shape control. Structural deformation of the aircraft should be measured at distributed sensor locations to ensure good controller performance. Shape sensing of aircraft structures using an inverse finite element (FE) method has been introduced by Tessler and Spangler [4]. First, a simplified three-dimensional (3D) structural model is created in this inverse FE method. Then, errors between measured and computed strain data are minimized using a numerical optimization technique. Deformation at distributed sensor locations are available from the tuned FE model. This approach, however, is useful primarily for off-line analysis because strain data continuously change during flight, and time-consuming structural optimizations are required whenever strain data are changed during unsteady motion. For the real-time shape sensing, closed-form equations for the computation of structural deformation from the measured strain data have been derived by Ko, Richards, and Tran [5]. Wing deflection along a line is available during flight using a systems such as the NASA Armstrong Flight Research Center Fiber Optic Sensing System (FOSS). Full field deformation, however, is not available, and deformation values are only available along the line of the FOSS installation [6, 7]. The two-step theory for a real-time shape sensing of a full 3D structure was introduced by Pak [8]. The first step is the computation of structural deformation along the neutral axis using a numerical integration of curvature (or strain) based on a linear least-squares method and cubic spline techniques. Curvature along the neutral axis is obtained using strain and the wing thickness information. This curvature is integrated twice to compute deformation along the neutral axis. The second step is to extrapolate deformation along the neutral axis, to the entire aircraft structure to obtain distributed deflection as well as slope information. Until now, this two-step theory has been demonstrated using simple plate-like structures [8, 9, 10].

The present study focuses on the application of this two-step theory to a wing with spars and ribs. Effects of the FE structural mesh density on the accuracy of wing shape computations are presented in this paper. In this study, the wing shape sensing technique previously developed [8] is applied to the X-59 QueSST aircraft (Lockheed Martin Corporation, Bethesda, Maryland), a tapered wing, a dihedral/anhedral wing, and a stiffened dihedral/anhedral wing.

III. Mathematical Background of the Two-step Theory

Deflection and slope of an entire 3D wing structure with spars and ribs are computed using the two-step theory [8] developed at the NASA Armstrong Flight Research Center.

A. The First Step: From Strain to Deformation Along the Neutral Axis

The first step is the computation of deformation along the neutral axis using an FE model independent method. Axial strains ϵ_u and ϵ_l, as shown in Fig. 1, obtained at the stations of the sensor lines on the upper and lower skins, respectively, are decomposed into strains due to in-plane and pure bending loads as given in Eqs. (1) and (2).

$$\epsilon_u = (\epsilon_u - \epsilon_l)/2 + (\epsilon_u + \epsilon_l)/2 \tag{1}$$

$$\epsilon_l = -(\epsilon_u - \epsilon_l)/2 + (\epsilon_u + \epsilon_l)/2 \tag{2}$$

In Eqs. (1) and (2), the strain due to in-plane load is $(\epsilon_u + \epsilon_l)/2$ and the strain due to pure bending load is $(\epsilon_u - \epsilon_l)/2$ and $-(\epsilon_u - \epsilon_l)/2$. Therefore, the curvature κ due to pure bending can be defined in Eq. (3).

$$\kappa(s) \equiv -\frac{(\epsilon_u - \epsilon_l)/2}{h/2} = -\frac{\epsilon_u(\tilde{s}) - \epsilon_l(\tilde{s})}{h(\tilde{s})} \tag{3}$$

where, $\tilde{s}$ is distance along the sensor line and $h(\tilde{s})$ is the wing thickness at $\tilde{s}$. The radius of the optical fiber sensor line in Fig. 1 is assumed to be very small compared with the wing thickness. Grid points, defining the neutral axis in Fig. 1, are created and connected to the grids at the upper and lower sensor lines using an interpolation finite element (RBE3 in the MSC/NASTRAN [11] terminology).

The first step of the two-step theory is summarized as follows [8]:

a. Fit the curvature data in Eq. (3) using the piecewise least-squares curve fitting method to minimize noise in measured data. This fitting is performed using a "Fiber coordinate system" shown in Fig. 2(a).
b. Obtain a cubic spline function using re-generated curvature data points, Eq. (4).

$$\frac{d^2 w(\tilde{s})}{d\tilde{s}^2} = \kappa(\tilde{s}) \tag{4}$$

A small motion assumption is used in Eq. (4).

c. Compute $\theta(\tilde{s}) = \frac{dw(\tilde{s})}{d\tilde{s}}$ and $w(\tilde{s})$ using slope and deflection boundary conditions at $\tilde{s} = 0$ together with the numerical integration routines.
d. Collect deformation data $\theta(\tilde{s})$ and $w(\tilde{s})$ along each neutral axis.

A local coordinate system, shown in Fig. 2(b), is introduced for the application of the two-step theory to a wing with taper or dihedral/anhedral effects. Deformations in tangential and normal direction to s coordinate in Fig. 2(b) are computed using Eqs. (5) and (6).

$$\Delta s = -w(\tilde{s}) \times sin\alpha \tag{5}$$

$$\Delta z = w(\tilde{s}) \times cos\alpha \tag{6}$$

where α in Eqs. (5) and (6) is a local angle due to a wing taper or dihedral/anhedral effects shown in Fig. 2(b). Finally, the local deformation Δs in Eq. (5) can be transformed to the global coordinate system shown in Fig. 2(c) using Eqs. (7) and (8).

$$\Delta x = -w(\tilde{s}) \times sin\alpha \times cos\beta \tag{7}$$

$$\Delta y = -w(\tilde{s}) \times sin\alpha \times sin\beta \tag{8}$$

In Eqs. (7) and (8), β is a local sweep angle due to curvilinear sensor line effects.

B. The Second Step: From Deformation Along the Neutral Axes to Full Field Deformation

In the second step, computed deflections along the neutral axes are fitted using a least-squares surface fitting technique, the System Equivalent Reduction and Expansion Process (SEREP) [12]. In this procedure, mode shapes from a modal analysis of an FE model are used as basis functions of the SEREP technique.

Re-arrange all the degrees of freedom (DOF) in the FE model as in Eq. (9), using the master DOF $\{\boldsymbol{q_M(t)}\}$ and slave DOF $\{\boldsymbol{q_S(t)}\}$:

$$\{\boldsymbol{q(t)}\} = \begin{Bmatrix} \boldsymbol{q_M(t)} \\ \boldsymbol{q_S(t)} \end{Bmatrix} \tag{9}$$

Deflections and slopes along the neutral axes obtained from the first step are defined as the measured master DOF $\{\boldsymbol{\tilde{q}_M(t)}\}$. The remaining deflections and slopes over the entire structure are defined as slave DOF. Consider the following coordinate transformation for the model reduction and expansion techniques as Eq. (10):

$$\begin{Bmatrix} \boldsymbol{q_M(t)} \\ \boldsymbol{q_S(t)} \end{Bmatrix} = [\boldsymbol{T}]\{\tilde{\boldsymbol{q}}_{\boldsymbol{M}}(\boldsymbol{t})\} \tag{10}$$

The $\boldsymbol{q_M(t)}$ in Eq. (10) is the fitted master DOF. Small measurement noise exists in the measured master DOF $\{\tilde{\boldsymbol{q}}_{\boldsymbol{M}}(\boldsymbol{t})\}$ that can be filtered out with a least-squares surface fitting technique [10]. From SEREP, the transformation matrix $[\boldsymbol{T}]$ can be expressed as Eq. (11):

$$[\boldsymbol{T}] = \begin{bmatrix} \boldsymbol{\Phi_M}\left(\boldsymbol{\Phi_M^{\mathrm{T}}\Phi_M}\right)^{-1}\boldsymbol{\Phi_M^{\mathrm{T}}} \\ \boldsymbol{\Phi_S}\left(\boldsymbol{\Phi_M^{\mathrm{T}}\Phi_M}\right)^{-1}\boldsymbol{\Phi_M^{\mathrm{T}}} \end{bmatrix} \tag{11}$$

where, $\boldsymbol{\Phi_M}$ and $\boldsymbol{\Phi_S}$ are eigen-matrices corresponding to master and slave DOFs, respectively. These eigen-matrices are computed from an FE model of the test article using the MSC/NASTRAN code. All the DOF in the structure can be computed using Eq.(12):

$$\{\boldsymbol{q(t)}\} = \begin{Bmatrix} \boldsymbol{q_M(t)} \\ \boldsymbol{q_S(t)} \end{Bmatrix} = \begin{bmatrix} \boldsymbol{\Phi_M}\left(\boldsymbol{\Phi_M^{\mathrm{T}}\Phi_M}\right)^{-1}\boldsymbol{\Phi_M^{\mathrm{T}}} \\ \boldsymbol{\Phi_S}\left(\boldsymbol{\Phi_M^{\mathrm{T}}\Phi_M}\right)^{-1}\boldsymbol{\Phi_M^{\mathrm{T}}} \end{bmatrix} \{\tilde{\boldsymbol{q}}_{\boldsymbol{M}}(\boldsymbol{t})\} \tag{12}$$

IV. Results and Discussions

The two-step theory for wing shape sensing summarized immediately above is applied in this section using FE models of the following sample cases: IV-A) the X-59 QueSST aircraft; IV-B) a tapered wing; IV-C) a dihedral/anhedral wing; and IV-D) a stiffened dihedral/anhedral wing. The first step of the two-step theory is used for the computation of structural deformation of the first three sample cases. The full field deformation is obtained with the last sample case to reduce the amount of result data in this section.

A. The X-59 QueSST Aircraft

The first sample case is based on an earlier version of an FE model of the X-59 QueSST aircraft with delta wing configuration (the C607 model) shown in Fig. 3. In this study, the sensor line pairs are assumed to be installed along the spar line near the center of gravity (CG) location (the blue lines in Fig. 3). The sensor line pairs, one on the upper skin and the other on the lower skin, along the current spar are designated as sensor lines 1 and 2, respectively. The trim load at Mach 1.42 cruise flight condition is applied to the C607 model.

Curvature distributions along the $\tilde{s}$ axis are obtained first from the upper and lower strain data shown in Fig. 4(a). These curvatures in Fig. 4(b) are integrated with respect to the $\tilde{s}$ axis twice using boundary conditions at the starting location and transformed to the global coordinate to have slope and deflection information, shown in Figs. 4(c) and 4(d), respectively. Wing tip differences between the two-step theory and the MSC/NASTRAN computation for slope and deflection are -11.2% and -19.8%, respectively. Large differences are observed in this case. Curvature distribution using the two-step theory and the MSC/NASTRAN results are compared in Fig. 4(b). The MSC/NASTRAN results are based on the numerical derivative of the splined slope distribution along the neutral axis. It can be concluded from Fig. 4(b) that the basic trend of the curvature distributions computed from Eq. (3) follow the MSC/NASTRAN results. Therefore, the curvature definition in Eq. (3), coordinate transformations in Eqs. (5) through (8), or the FE structural model in Fig. 3, are re-examined.

The two-step theory used in this study to compute a wing deformation is based on integration of curvature (or strain) distribution from the wing root section to the wing tip section. Therefore, small deflection difference near the wing root section, Fig. 4(b), can be propagated to the wing tip deflection. Wing slope difference near the wing root section is large, as shown in Fig. 4(c). To quantify the differences introduced by curvature inaccuracy at the wing root, the results of the two-step theory applied to the strain data along the sensor lines 1 and 2, except strain values near the wing root section, are shown in Fig 5. Slope and deflection differences between the MSC/NASTRAN and the two-step theory results at the wing tip section are -2.02% and -4.97%, respectively. Therefore, the curvature inaccuracy near the wing root area contributes significantly to the wing deformation predicted at the wing tip area.

Detailed internal structural layout near the wing root is also shown in Fig. 3. It should be noted in Fig. 3 that a stiffening structure, illustrated by a pink line, is used between wing ribs 1 and 2. This stiffening structure crosses the spar where sensor lines 1 and 2 are located. Another spar where sensor lines 3 and 4 are located, illustrated by green lines in Fig. 3, is selected as the next sample test case to investigate the source of the modeling issue observed over sensor lines 1 and 2. Results based on sensor lines 3 and 4 are shown in Fig. 6. In this case, wing tip differences between the two-step theory and the MSC/NASTRAN code for slope and deflection computations are drastically

reduced to -1.91% and -6.63%, respectively. Therefore, it is concluded that the strain data may be affected by the illustrated stiffening structure.

B. The Tapered Wing

A tapered aluminum wing example was prepared to investigate the curvature observed with the X-59 QueSST model. The tapered wing has root and tip chord lengths of 70 and 35 inches, respectively, and a half-span length of 400 inches, as shown in Fig. 7. The wing thickness at the wing tip is also the half of the thickness at the wing root. Eight ribs are located every 50 inches except at the wing root section. The four spars are located 4, 22, 40, and 58 inches from the leading edge of the wing root section. Detailed properties of this tapered wing are presented in Table 1. The red line beam elements in Fig. 7 represent sensor line elements modeled with zero stiffness and zero weight. Images of FE models of two different mesh densities, called "coarse mesh" and "fine mesh", are also depicted in Fig. 7. A one-G load is applied to this tapered wing. The FE grids, defining the neutral axis between each pair of upper and lower sensor lines, are created using grids located at the upper and lower sensor lines and RBE3 elements. Deflections along these neutral axes will become a measured DOF, $\{\tilde{\boldsymbol{q}}_{\boldsymbol{M}}(\boldsymbol{t})\}$, for the second step.

The strain data along the sensor lines 1 and 2 from the fine mesh are shown in Fig. 8(a). First, curvature values in Fig. 8(b) are computed using Eq. (3). The MSC/NASTRAN based curvature values are computed through the use of a numerical derivative of the splined angle distribution along the neutral axis, shown in Fig. 8(c). The Fig. 8(b) plots shows that the curvature distribution between each rib location obtained from the two-step theory is an excellent match with the MSC/NASTRAN results. The curvature difference at the rib locations might be affected by the numerical derivative of the splined angle or caused by insufficiently fine mesh sizing near each rib. Deflection distribution along the neutral axis is given in Fig. 8(d). Slope and deflection distribution obtained from the two-step theory are in excellent match with the MSC/NASTRAN results, as shown in Figs. 8(c) and 8(d). The percentage differences of slope and deflection at the wing tip from the two-step theory and the MSC/NASTRAN code are -0.019% and -0.046%, respectively.

Next, results based on the coarse mesh are presented in Fig. 9. It should be noted in Figs. 8(a) and 9(a) that the upper and lower strain data are not drastically changed, and therefore the curvature distributions in Figs. 8(b) and 9(b) have similar trends. Therefore, the percentage differences of slope and deflection at the wing tip from the two-step theory and the MSC/NASTRAN code are -0.036% and -0.066%, respectively. It can be concluded in the tapered wing case that the two-step theory results match excellently with MSC/NASTRAN results even when using a coarse mesh FE model.

C. The Dihedral/Anhedral Wing

The delta wing of the X-59 QueSST aircraft has dihedral and anhedral effects, and therefore dihedral and anhedral effects (as shown in Fig. 10) are added to the tapered wing analyzed immediately above. The span-wise shape of the wing (looking from the front), along with coarse or fine mesh FE models of this wing are shown in Fig. 10.

Results based on the fine mesh FE model are shown in Fig. 11. The curvature, slope, and deflection along the neutral axis are computed using strain data from sensor lines 1 and 2 in Fig. 10. Wing tip differences of slope and deflection computed from the two-step theory and the MSC/NASTRAN code are -0.603% and -0.779%, respectively. The dihedral/anhedral wing results have larger differences than the tapered wing case, which may be caused by inaccurate strain data near rib and spar intersections. The strain data near rib and spar intersections are not continuous, as shown in Fig. 11(a). Therefore, an even finer mesh is required to produce continuous strain data at these locations. The curvature distribution from the two-step theory and the MSC/NASTRAN code are in excellent match between each rib as shown in Fig. 11(b). It can be concluded in Figs. 11(c) and 11(d) that the slope and deflection obtained from the two-step theory are also in good match with the MSC/NASTRAN results.

Next, the coarse mesh FE model results are presented (Fig. 12). Unlike the fine mesh results in Fig. 11(a), the upper and lower strain data in Fig. 12(a) demonstrate simple and monotonic behavior. Therefore, curvature distributions in Fig. 12(b) are also simple and monotonic. Rib effects, previously noted in Fig. 11(b), are not observed in Fig. 12(b). It should be noted that the curvatures computed from the two-step theory and the MSC/NASTRAN code are in good agreement even between the root chord and the first two ribs. Slope and deflection differences at the wing tip section obtained from the two-step theory and the MSC/NASTRAN code are -0.548% and -0.794%, respectively, as shown in Figs. 12(c) and 12(d).

The strain data from the coarse mesh case, Fig. 12(a), are close to the average values of the strain data obtained from the fine mesh case, Fig. 11(a). Therefore, the curvature values computed from the coarse and fine meshes exhibit similar trends, as shown in Figs. 11(b) and 12(b). The effects of the ribs, however, are not correctly captured with the coarse mesh; therefore, a fine mesh is necessary to capture accurate curvature distribution. In general, the deformation results obtained from the coarse mesh FE model are good enough. In this study, it can be concluded from Figs. 9(c),

9(d), 12(c), and 12(d) that the two-step theory using the coarse mesh FE models perform a good-enough shape prediction of the tapered and dihedral/anhedral wings.

D. The Stiffened Dihedral/Anhedral Wing

As shown above in section IV-A, "The X-59 QueSST Aircraft," differences of deflection and slope at the wing tip section are strongly affected by the existence of a stiffening structure near the wing root area. To study this effect, a stiffening structure was added near the wing root section of the dihedral/anhedral wing as shown in Fig. 13. Coarse, intermediate, and fine meshes were used for the stiffened dihedral/anhedral wing case.

The strain, curvature, slope, and deflection distributions using the coarse mesh FE model are shown in Fig. 14. Rib effects are not observed in the strain data in Fig. 14(a). In this case, the curvatures computed from the two-step theory and the MSC/NASTRAN code do not match between the root chord and first two rib locations of the stiffened dihedral/anhedral wing, as shown in Fig. 14(b). The curvatures are, however, in good match between span stations of 100 and 400 inches. It should be noted that the stiffening structure between span stations of 0 and 100 inches creates an irregular structural shape. On the other hand, periodic structural shape is observed between span stations of 100 and 400 inches. Slope and deflection differences at the wing tip section obtained from the two-step theory and the MSC/NASTRAN code are -7.27% and -10.2%, respectively, as shown in Figs. 14(c) and 14(d).

The intermediate mesh FE model simulation results with the stiffened dihedral/anhedral wing are presented in Fig. 15. In this case, the effect of ribs is clearly observed in the upper and lower strain data, Fig. 15(a). The curvatures computed using Eq. (3) match well with the curvatures obtained from the MSC/NASTRAN results, as shown in Fig. 15(b). The slope and deflection differences at the wing tip section computed from the two-step theory and the MSC/NASTRAN code are -0.535% and -0.694%, respectively, as shown in Figs. 15(c) and 15(d). The differences are drastically reduced when the intermediate mesh FE model is used for the wing shape sensing of the stiffened dihedral/anhedral wing.

Finally, the fine mesh FE model is used to study the wing shape sensing problem. In this case, the effect of the ribs was clearly observed in the upper and lower strain data, shown in Fig. 16(a). Curvatures from the two-step theory match excellently with the corresponding MSC/NASTRAN results, as shown in Fig. 16(b). The slope and deflection differences at the wing tip section become -0.564% and -0.796%, respectively.

It is concluded that in general a fine mesh FE model is desired for accurate prediction of wing shape and curvature distribution. In case of an FE model with a regular rib configurations, even a coarse mesh FE model may provide acceptable strain data and wing shape sensing, however, a fine mesh FE model is required for the pre-test analysis of aircraft such as the X-59 QueSST aircraft.

A three-dimensional wing shape is obtained using Eq. (8) together with the y, z, and roll deformations computed from the first step, $\{\tilde{\boldsymbol{q}}_{\boldsymbol{M}}(\boldsymbol{t})\}$. In this study, values of the measured master DOF $\{\tilde{\boldsymbol{q}}_{\boldsymbol{M}}(\boldsymbol{t})\}$ are based on the results from the fine mesh FE model. However, the coarse mesh and the intermediate mesh FE models are used for the computations of the basis shapes $\boldsymbol{\Phi}_{\boldsymbol{M}}$ and $\boldsymbol{\Phi}_{\boldsymbol{S}}$ because of speed and memory limitation of the computer. Table 2 provides the number of DOF information of $\{\tilde{\boldsymbol{q}}_{\boldsymbol{M}}(\boldsymbol{t})\}$ (or $\{\boldsymbol{q}_{\boldsymbol{M}}(\boldsymbol{t})\}$) and $\{\boldsymbol{q}_{\boldsymbol{S}}(\boldsymbol{t})\}$ for each mesh. In this study, the first six flexible mode shapes are selected as the basis shapes. Deformations at the wing tip section are summarized in Table 3. It should be noted in Table 3 that the percentage differences after the second step are smaller than the first step. This may be due to the effect of the least-squares surface fitting technique, SEREP. In Table 3, the step 1 and step 2 results are $\{\tilde{\boldsymbol{q}}_{\boldsymbol{M}}(\boldsymbol{t})\}$ and $\{\boldsymbol{q}_{\boldsymbol{M}}(\boldsymbol{t})\}$ values in Eq. (8), respectively. Graphical comparison of the z deflections at the wing tip and typical sections are given in Fig. 17. It is concluded that the two-step theory predicts wing shape correctly at each cross section. The smooth wing shape prediction is accomplished in this study as shown in Fig. 18.

V. Conclusion

A finely meshed finite element (FE) structural model is desired to capture accurate curvature distributions along the neutral axes of wing cross sections during pre-test analysis for strain based shape sensing of a wing with ribs and spars. In the case of an FE model with a regular rib configuration, such as the tapered wing and the dihedral/anhedral wing in this study, coarser mesh FE models may provide acceptable strain data and deflection and slope information. There is no guarantee, however, that strain data obtained from the coarse mesh FE simulation are acceptable. A fine mesh FE model may be necessary to obtain accurate curvature distribution. A finely meshed FE model is required for the pre-test analysis of complex aircraft wing configurations such as the low-boom flight demonstration aircraft.

The two-step theory used in this study performs excellently for the wing shape sensing of the tapered wing, the dihedral/anhedral wing, and the stiffened dihedral/anhedral wing. The curvature equation based on the decomposition of the in-plane strain and pure bending strain was successfully applied to the wing with spars and ribs.

It should be noted that the percentage differences after the second step of the two-step theory are smaller than those of the first step, perhaps due to the effect of the least-squares surface fitting technique, System Equivalent Reduction and Expansion Process (SEREP).

Acknowledgments

The work presented in this paper was funded by the Low-Boom Flight Demonstration Project under the NASA Aeronautics Research Mission Directorate. The author thanks peer review committee members Frank Pena, Roger Truax, and Keerti Bhamidipati of the NASA Armstrong Flight Research Center.

Tables

Table 1. Properties of the tapered wing.

Material	Aluminum
Half span length	400 inch
Root chord length	70 inch
Tip chord length	35 inch
Space between each rib	50 inch (no rib at root chord)
Chord-wise locations of spars at root chord	4, 22, 40, and 58 inch
Upper and lower skin thickness	0.05 inch
Thickness of ribs	0.1 inch
Thickness of leading- and trailing-edge spars	0.1 inch
Thickness of two center spars	0.2 inch

Table 2. Number of degrees of freedom for finite element models of the stiffened dihedral/anhedral wing.

Mesh	**Number of degrees of freedom**		
	Total DOF $\{q_M(t)\}$+$\{q_S(t)\}$	**Master DOF $\{\tilde{q}_M(t)\}$**	**Slave DOF $\{q_S(t)\}$**
Coarse	1,356	51	1,305
Intermediate	21,192	972	20,220
Fine	2,240,442	2,403	2,238,039

Table 3. Deformation of the stiffened dihedral/anhedral wing at the wing-tip section.

Deformation	**Target**	**Step 1 (fine mesh)**		**Step 2 (coarse mesh)**		**Step 2 (intermediate mesh)**	
		Value	% difference	Value	% difference	Value	% difference
X	-0.06057	N/A	N/A	-0.05113	-15.6	-0.05571	-8.02
Y	-0.1740	-0.1821	**4.66**	-0.1725	**-0.86**	-0.1738	**-0.11**
Z	-3.392	-3.365	**-0.80**	-3.367	**-0.74**	-3.368	**-0.71**
Roll	-0.01241	-0.01234	**-0.56**	-0.01234	**-0.56**	-0.01237	**-0.32**
Pitch	3.205E-4	N/A	N/A	2.924E-4	-8.77	3.019E-4	-5.80
Yaw	1.981E-4	N/A	N/A	1.601E-4	-19.2	1.820E-4	-8.13
Results are based on strains along the sensor lines 1 and 2.							

Figures

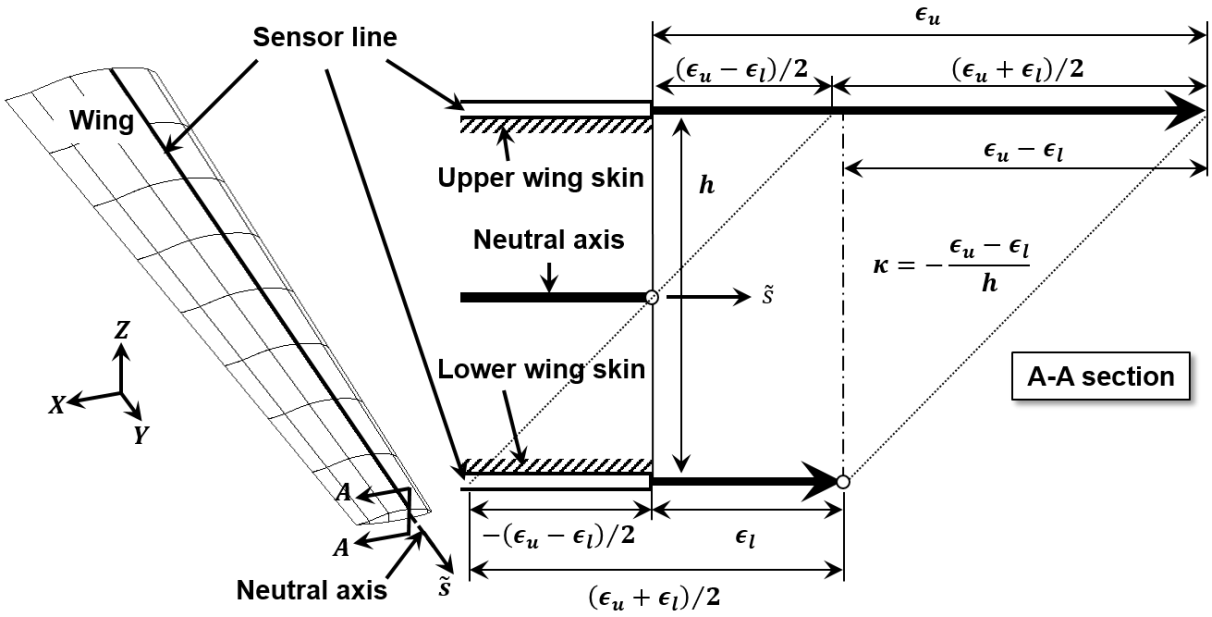

Fig. 1. Definition of curvature κ.

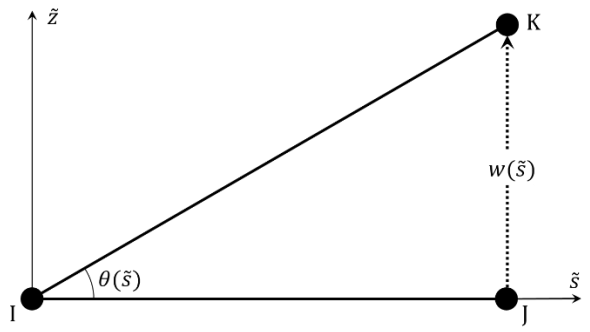

(a) Fiber coordinate ($\tilde{s}$,$\tilde{z}$)

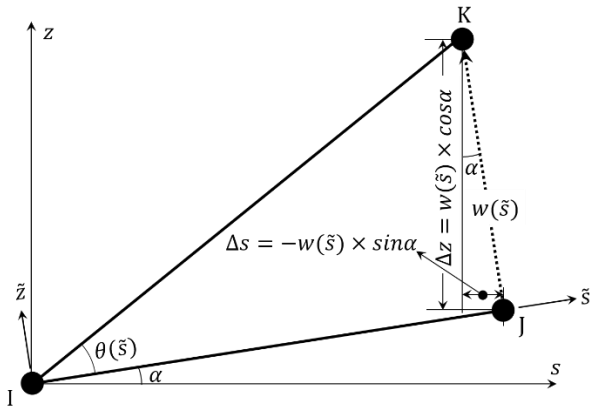

(b) Local coordinate (s,z)

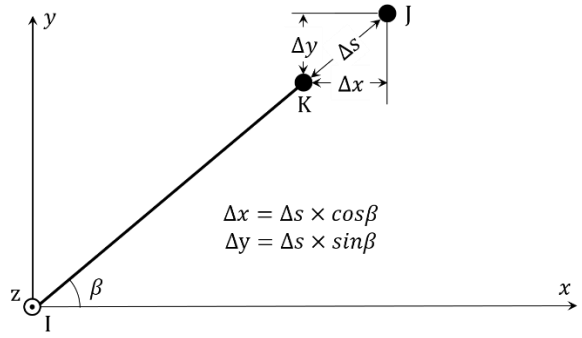

(c) Global coordinate (x, y, z)

Fig. 2. Coordinate systems for deformation computations.

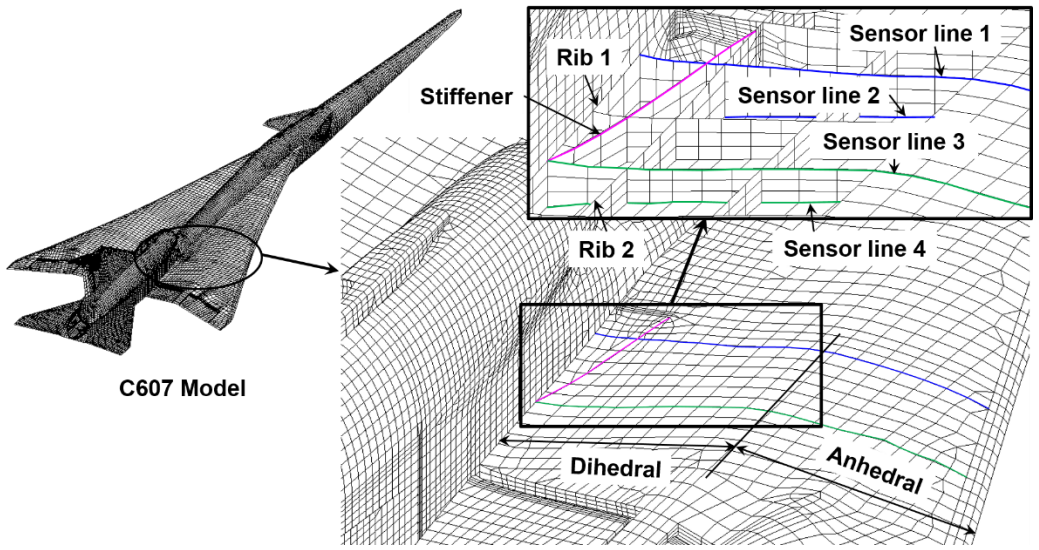

Fig. 3. Afinite element structural model of the X-59 QueSST (Lockheed Martin Corporation, Bethesda, Maryland) aircraft.

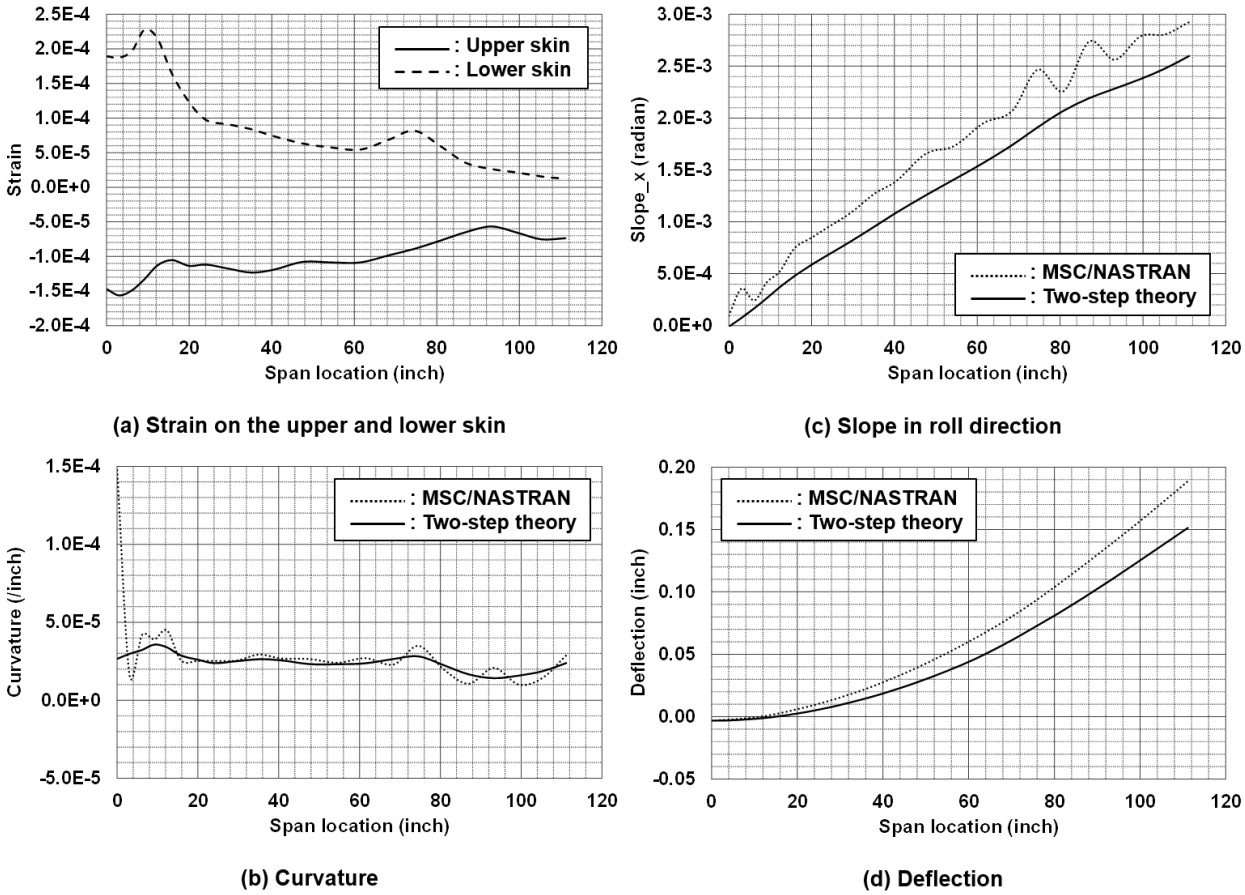

Fig. 4. Strain, curvature, and deformation of the X-59 QueSST aircraft (Lockheed Martin Corporation, Bethesda, Maryland) using data from sensor lines 1 and 2.

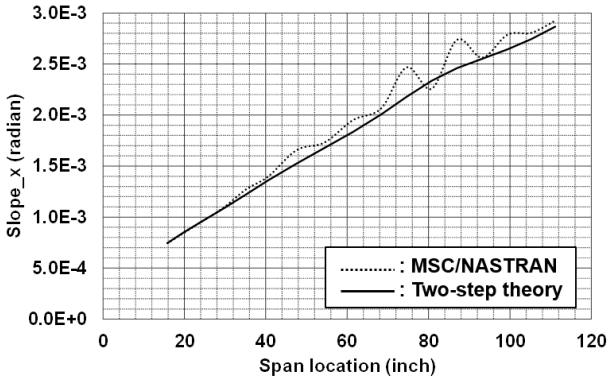

(a) Slope in roll direction

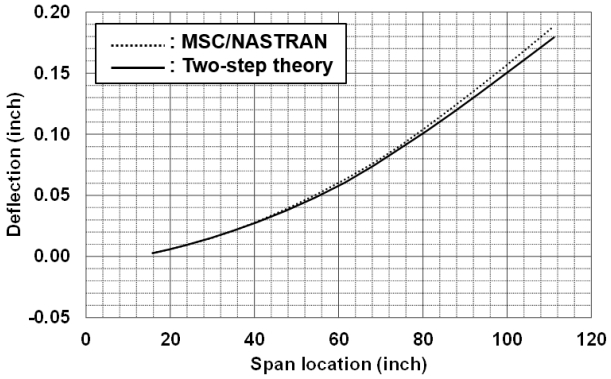

(b) Deflection

Fig. 5. Deformation of the X-59 QueSST aircraft (Lockheed Martin Corporation, Bethesda, Maryland) integrated from 18 inch using data from sensor lines 1 and 2.

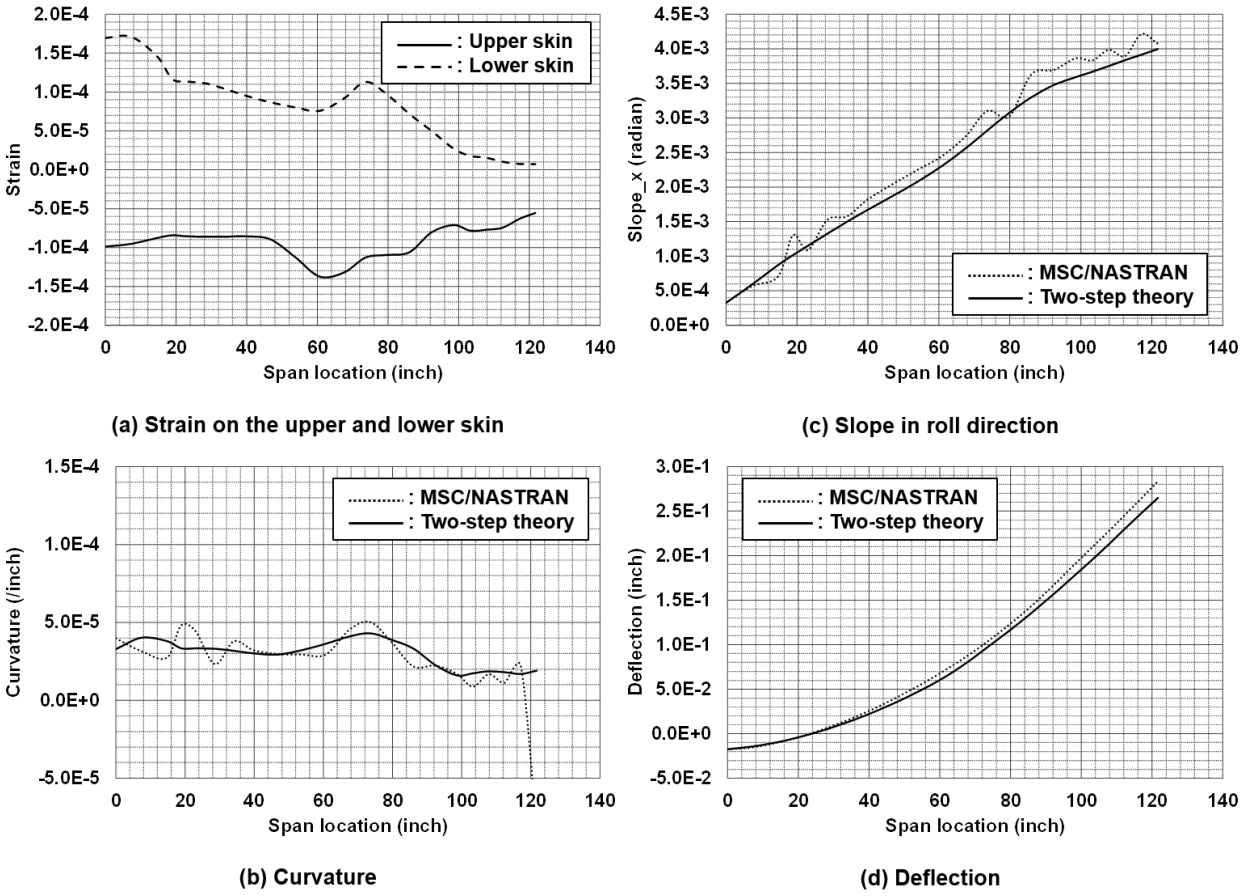

Fig. 6. Strain, curvature, and deformation of the X-59 QueSST aircraft (Lockheed Martin Corporation, Bethesda, Maryland) using data from sensor lines 3 and 4.

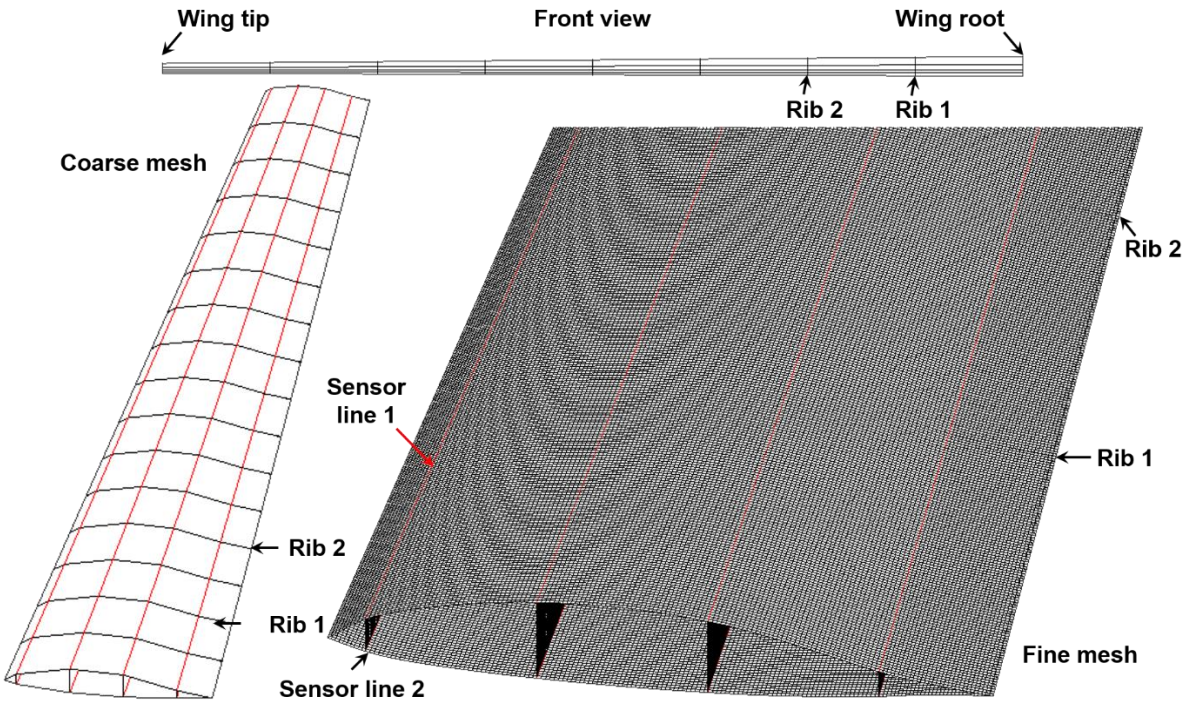

Fig. 7. The tapered wing with coarse and fine meshes.

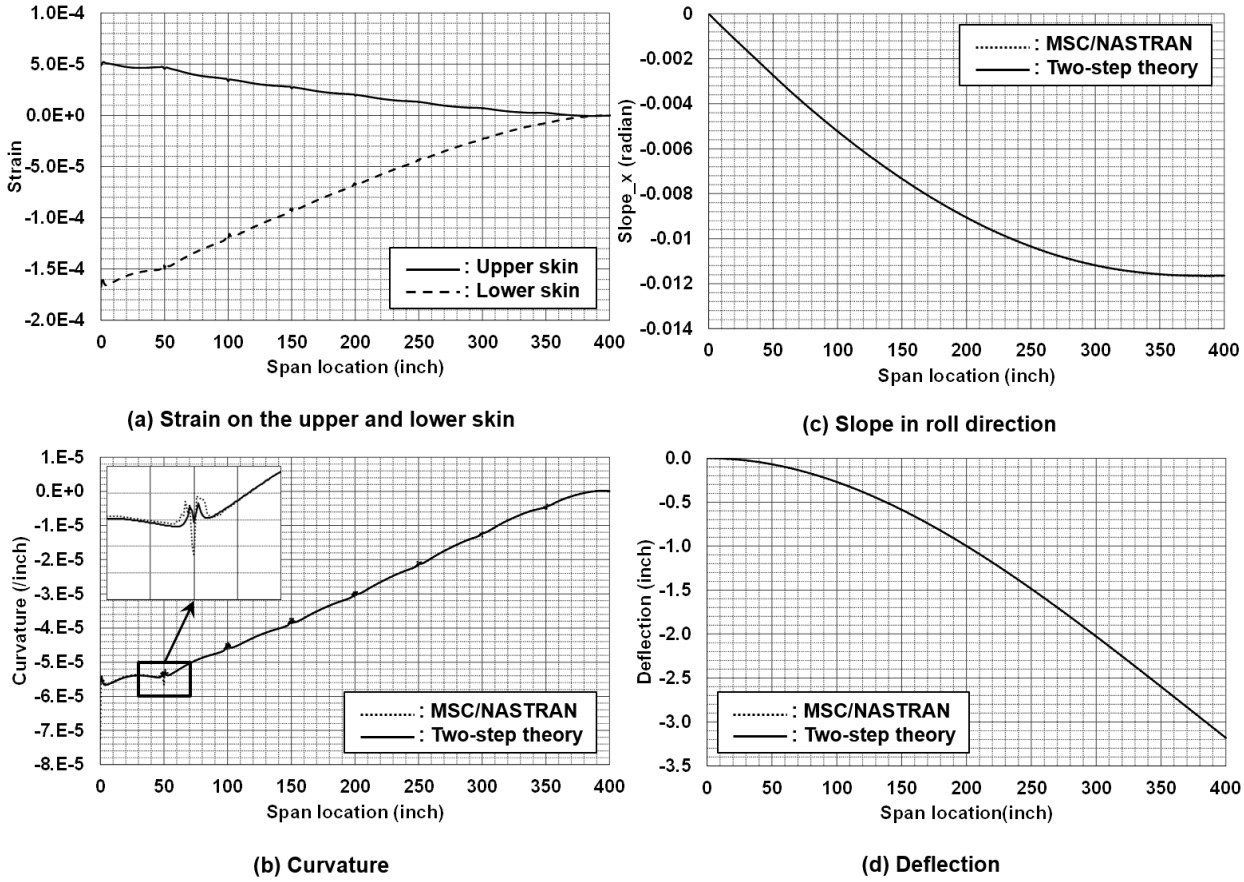

Fig. 8. The strain, curvature, and deformation of the tapered wing with fine mesh.

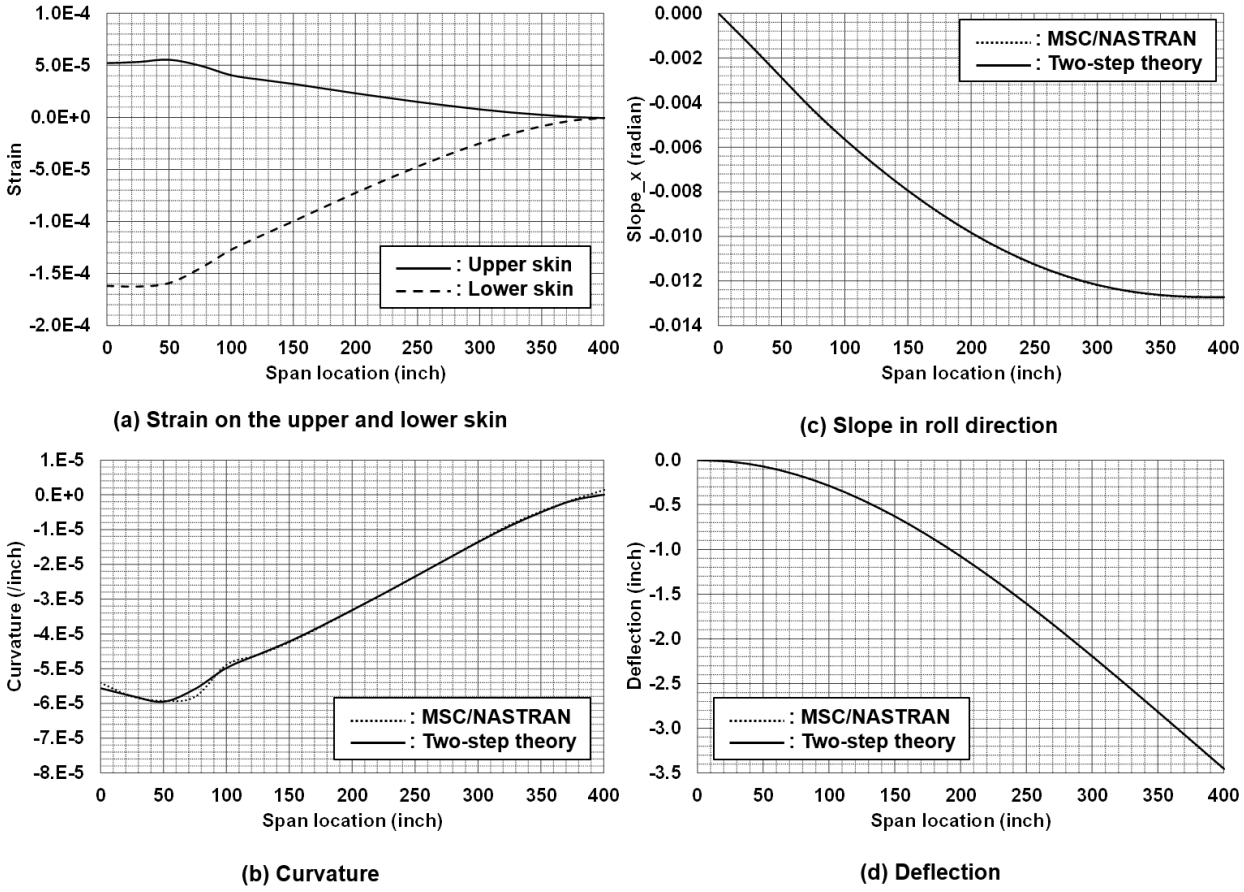

Fig. 9. The strain, curvature, and deformation of the tapered wing with coarse mesh.

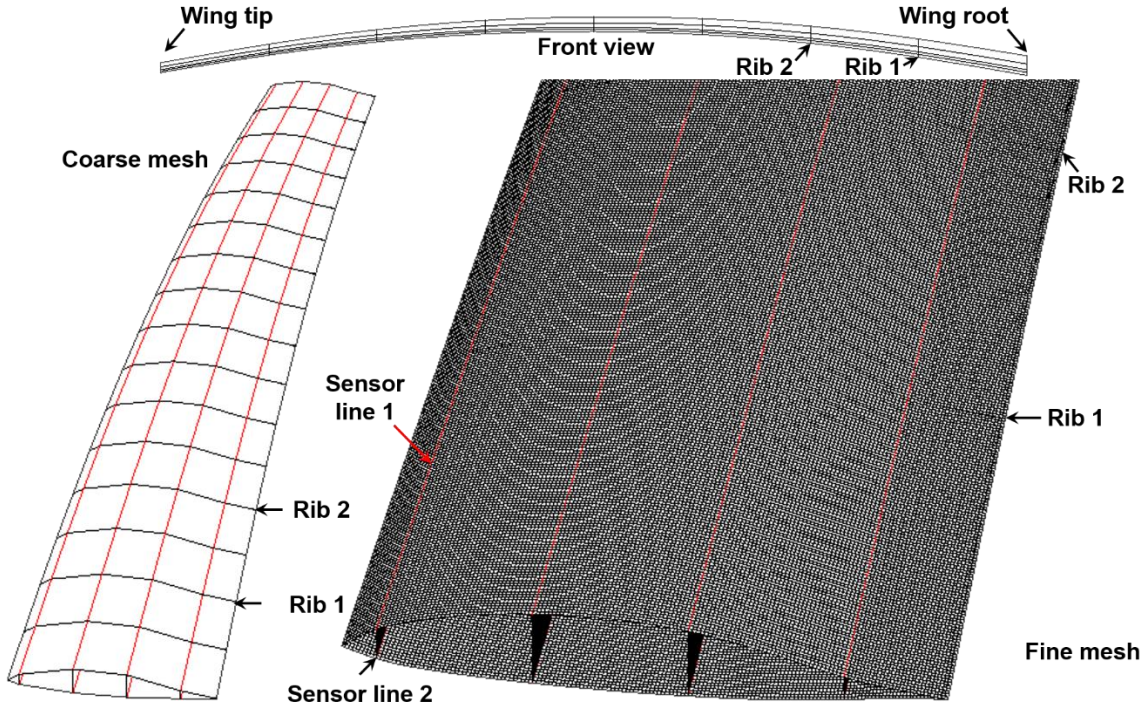

Fig. 10. The dihedral/anhedral wing with coarse and fine meshes.

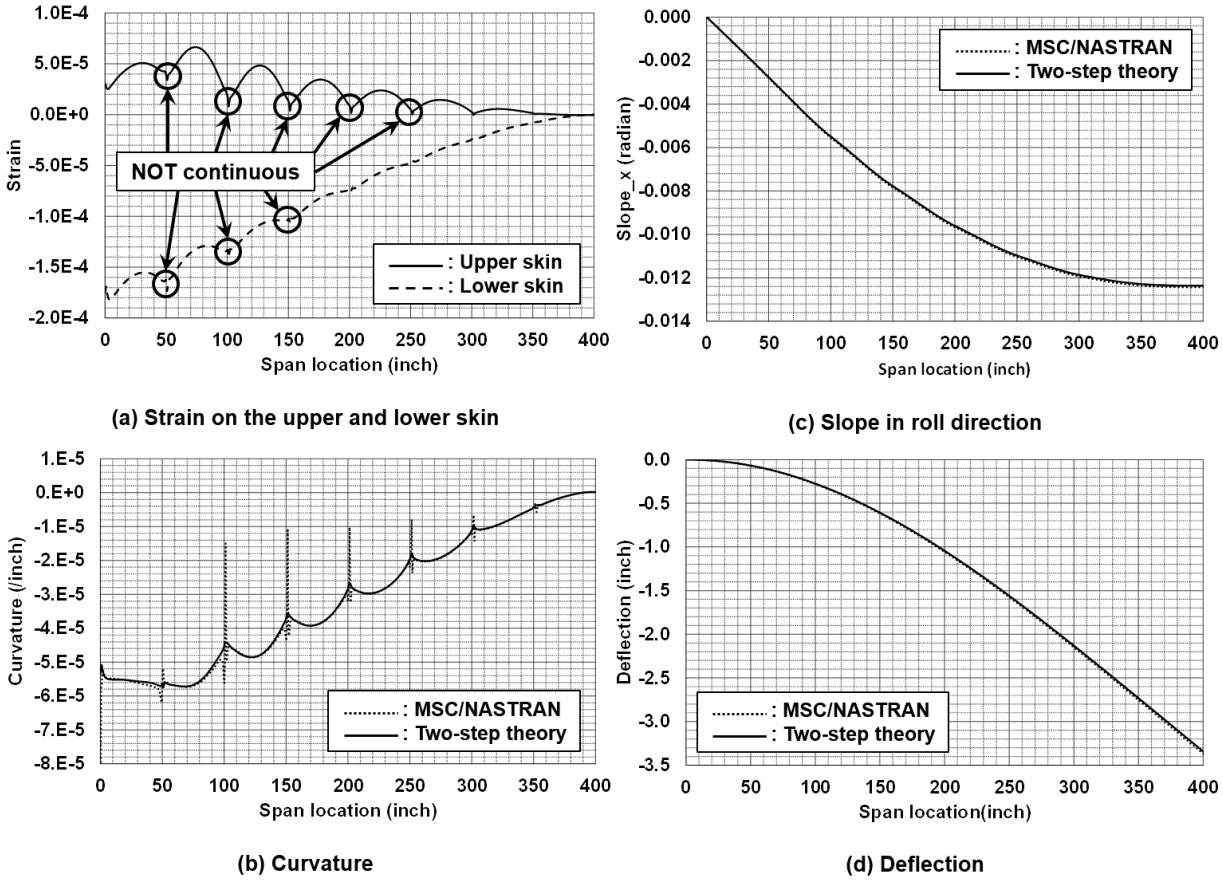

Fig. 11. The strain, curvature, and deformation of the dihedral/anhedral wing with fine mesh.

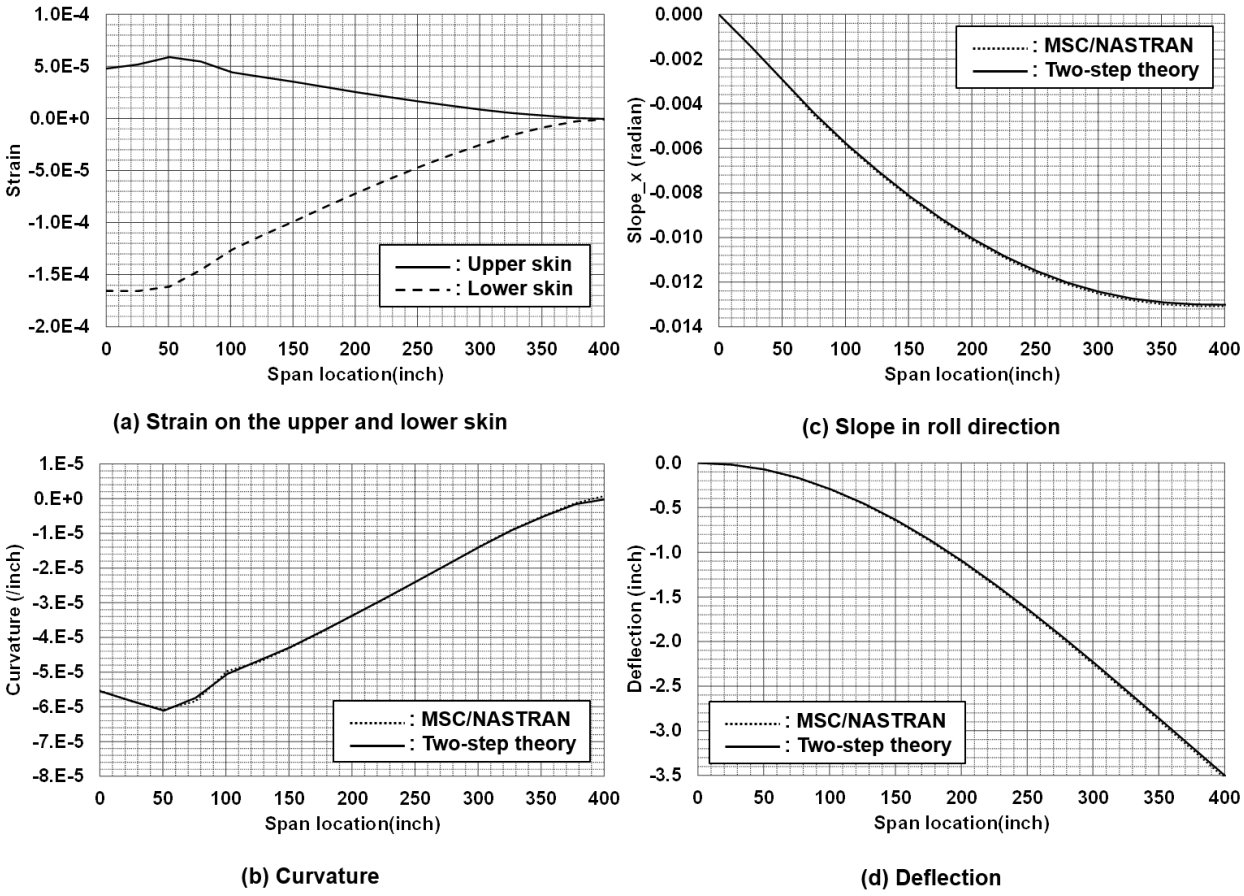

Fig. 12. The strain, curvature, and deformation of the dihedral/anhedral wing with coarse mesh.

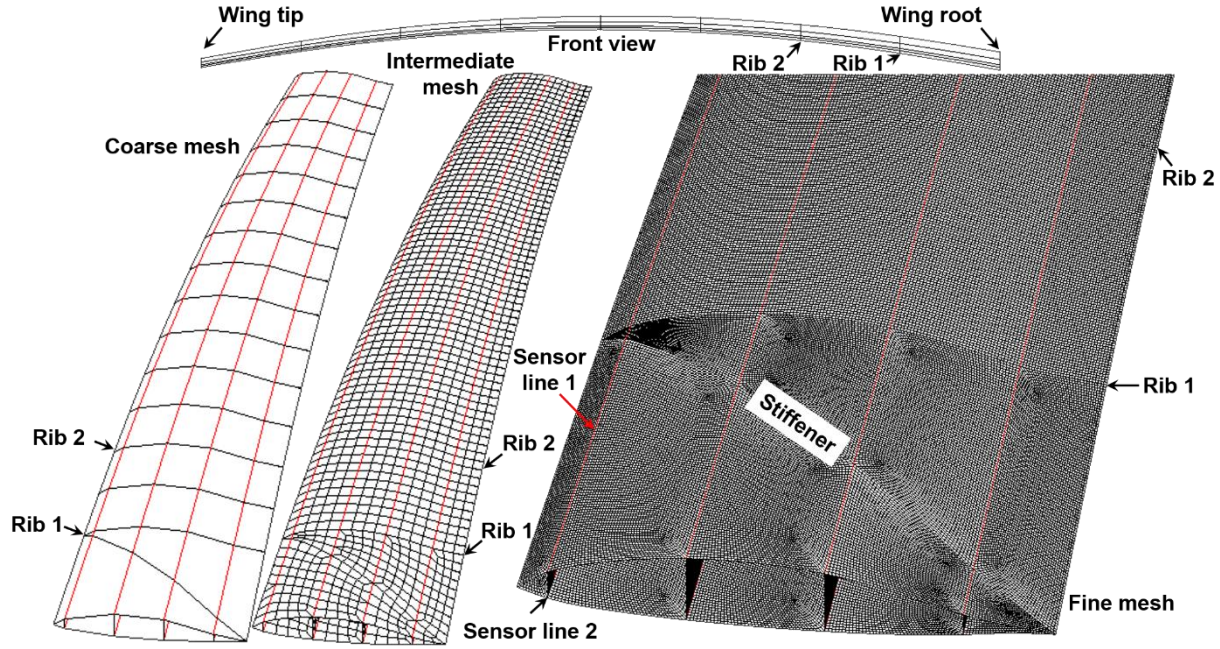

Fig. 13. The stiffened dihedral/anhedral wing with coarse, intermediate, and fine meshes.

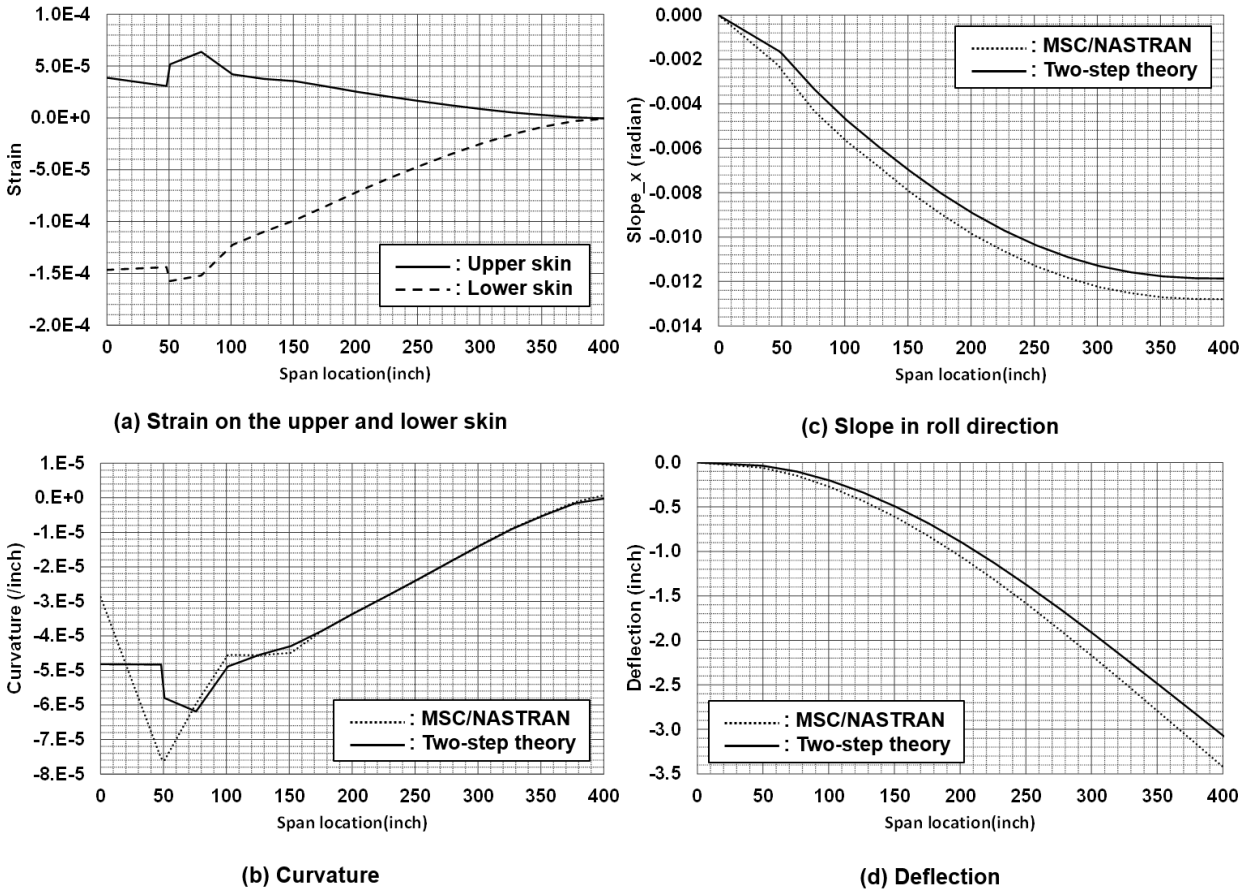

Fig. 14. The strain, curvature, and deformation of the stiffened dihedral/anhedral wing with coarse mesh.

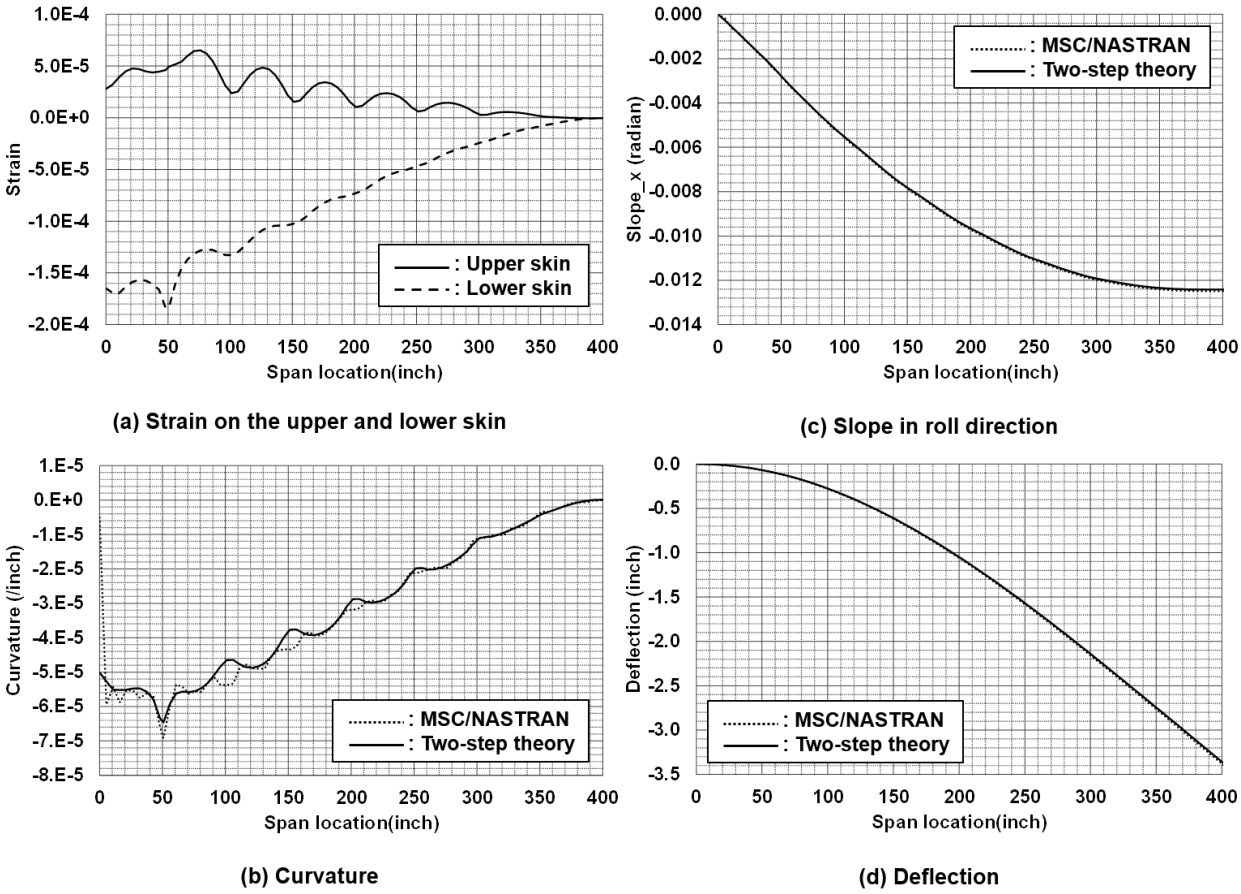

Fig. 15. The strain, curvature, and deformation of the stiffened dihedral/anhedral wing with intermediate mesh.

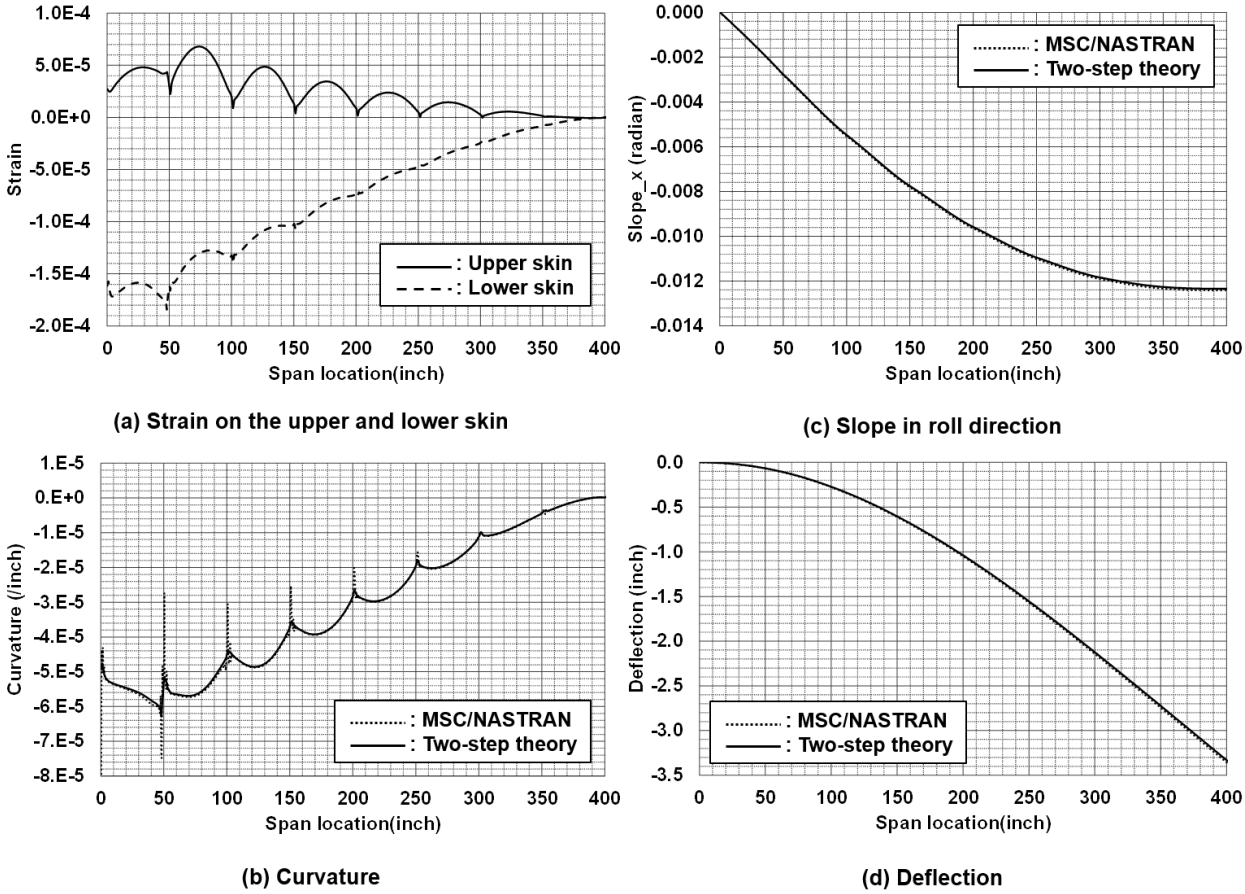

Fig. 16. The strain, curvature, and deformation of the stiffened dihedral/anhedral wing with fine mesh.

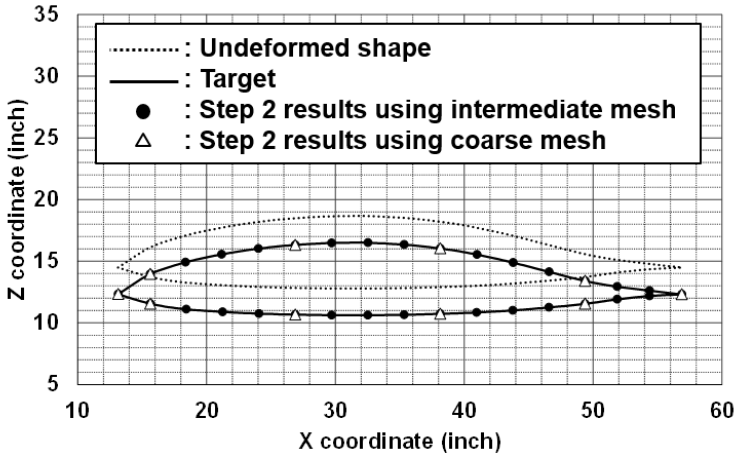

(a) At typical section

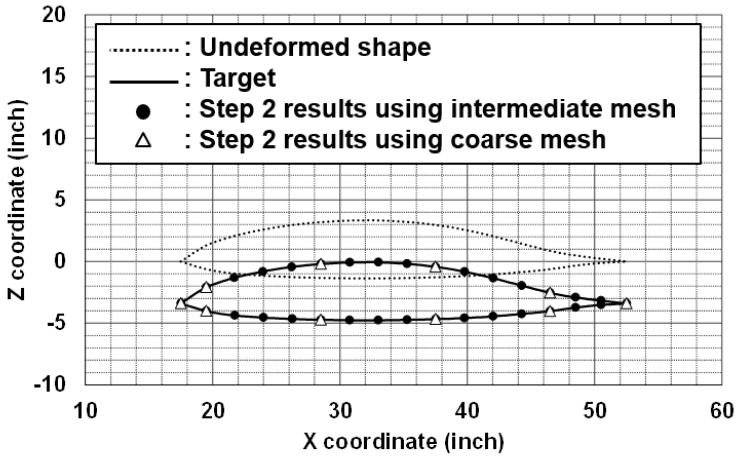

(b) At wing-tip section

Fig. 17. The chord-wise deflection of the stiffened dihedral/anhedral wing at typical and wing-tip sections.

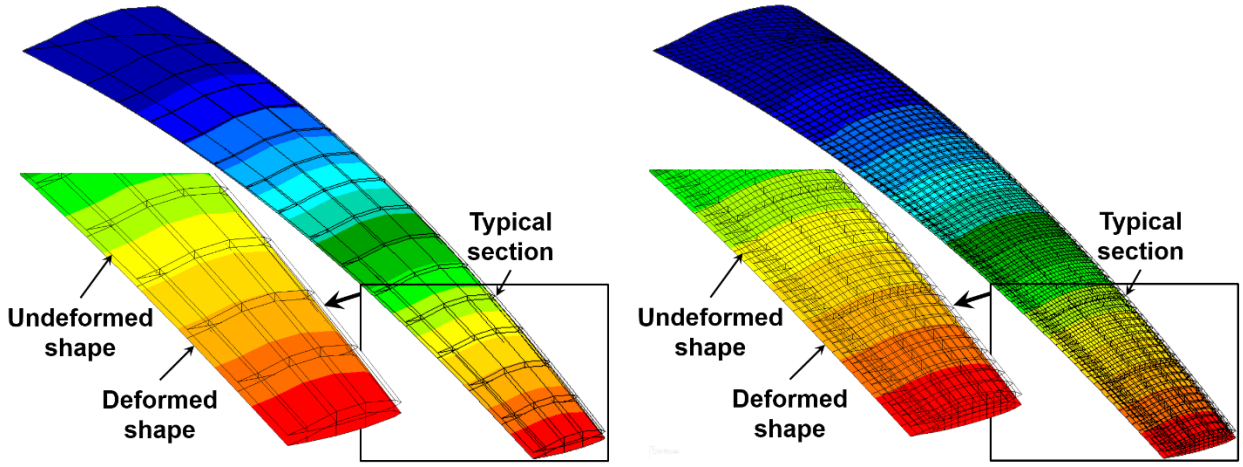

(a) Use coarse mesh for step 2 (b) Use intermediate mesh for step 2

Fig. 18. The deformation of the stiffened dihedral/anhedral wing after step 2.

References

[1] Noll, T. E., Brown, J. M., Perez-Davis, M. E., Ishmael, S. D., Tiffany, G. C., and Gaier, M., "Investigation of the Helios Prototype Aircraft Mishap, Volume I Mishap Report," NASA, 2004.

[2] Pak, C.-g., "Aeroelastic Tailoring Study of an N+2 Low-boom Supersonic Commercial Transport Aircraft," AIAA Paper 2015-2791, June 2015.
doi: 10.2514/6.2015-2791

[3] Pak, C.-g., "Jig-Shape Optimization of a Low-Boom Supersonic Aircraft," *Journal of Aircraft,* Vol. 55, No. 5, 2018, pp. 2154-2161.
doi: 10.2514/1.C034851.

[4] Tessler, A., and Spangler, J. L., "A Variational Principle for Reconstruction of Elastic Deformations in Shear Deformable Plates and Shells," NASA/TM-2003-212445, 2003.

[5] Ko, W. L., Richards, W. L., and Tran, V. T., "Displacement Theories for In-Flight Deformed Shape Predictions of Aerospace Structures," NASA/TP-2007-214612, 2007.

[6] Bakalyar, J., and Jutte, C., "Validation Tests of Fiber Optic Strain-Based Operational Shape and Load Measurements," AIAA Paper 2012-1904, April 2012.
doi: 10.2514/6.2012-1904

[7] Derkevorkian, A., Masri, S. F., Alvarenga, J., Boussalis, H., Bakalyar, J., and Richards, W. L., "Strain-Based Deformation Shape-Estimation Algorithm for Control and Monitoring Applications," *AIAA Journal,* Vol. 51, No. 9, 2013, pp. 2231-2240.
doi:10.2514/1.J052215

[8] Pak, C.-g., "Wing Shape Sensing from Measured Strain," *AIAA Journal,* Vol. 54, No. 3, 2016, pp. 1064-1073.
doi:10.2514/1.J053986

[9] Pak, C.-g., and Truax, R., "Acceleration and Velocity Sensing from Measured Strain," AIAA Paper 2016-1229, January 2016.
doi: 10.2514/6.2016-1229

[10] Pak, C.-g., "Unsteady Aerodynamic Force Sensing from Strain Data," *Journal of Aircraft,* Vol. 54, No. 4, 2017, pp. 1476-1485.
doi: 10.2514/1.C034140

[11] MSC/NASTRAN Quick Reference Guide Version 69, The MacNeal-Schwendler Corporation, Newport Beach, California, 1996.

[12] O'Callahan, J., Avitabile, P., and Riemer, R., "System Equivalent Reduction Expansion Process (SERP)," *Proceedings of the 7th International Modal Analysis Conference, Vol. 1,* 1989, pp. 29-37.